Sources of baroclinic tidal energy in the Gaoping Submarine Canyon off southwestern Taiwan

Ming-Da Chiou,[1] Sen Jan,[1] Joe Wang,[1] Ren-Chieh Lien,[2] and Hwa Chien[3]

Received 7 June 2011; revised 13 September 2011; accepted 5 October 2011; published 14 December 2011.

[1] A three-dimensional model driven by tidal constituents O_1, K_1, M_2 and S_2 was adopted to evaluate the sources of baroclinic tidal energy in the Gaoping Submarine Canyon (GPSC) off southwestern Taiwan. The model domain covered the probable primary generation sites, including the Luzon Strait (LS) and the southeastern Taiwan Strait (TS). The simulated baroclinic tides agreed with the observations of tidal current velocity, isotherm vertical displacement, and baroclinic tidal energy flux (F_{bc}) in the GPSC. The depth-integrated, seven-day-averaged F_{bc} computed from the model result was 2.2 kW m^{-1} in the GPSC, and the corresponding area-integrated F_{bc} reached 189.4 MW. The results obtained from the model suggest that the baroclinic tides lead to strong turbulent mixing near the canyon head with a vertical diffusivity of 3.5×10^{-3} m^2 s^{-1}. Baroclinic tidal energy in the GPSC is mainly generated on the western ridge in the LS and on the steep topography in the southeastern TS. The local generation of baroclinic energy only accounts for 4.4% of the total value. The other 95.6% of the baroclinic tidal energy is remotely generated at the LS and the southeastern TS of which 31.9% and 8.8% are directly emanated, respectively, into the GPSC. The northwestward and southeastward baroclinic energy beams radiating from the LS and the southeastern TS, respectively, meet each other and form internal partial standing tides outside the GPSC. The transverse baroclinic energy from the internal partial standing tides accounts for the remaining 54.9% of the baroclinic tidal energy in the GPSC.

Citation: Chiou, M.-D., S. Jan, J. Wang, R.-C. Lien, and H. Chien (2011), Sources of baroclinic tidal energy in the Gaoping Submarine Canyon off southwestern Taiwan, *J. Geophys. Res.*, *116*, C12016, doi:10.1029/2011JC007366.

1. Introduction

[2] Submarine canyons are major conduits for material and energy transport between the continental shelf and the deep ocean through both advection and mixing processes. The flow patterns in submarine canyons are complicated, due to a relatively high Rossby number and the presence of internal waves [*Allen and de Madron*, 2009; *Jordi et al.*, 2005; *Carter*, 2010]. Because of the unique topography, the energy sources of baroclinic tides (also called internal tides) may propagate shoreward from the open ocean along the thalweg of the canyon and may further generate at the peripheries of the canyon [*Baines*, 1982; *Petruncio et al.*, 2002; *Jachec et al.*, 2006]. *Hotchkiss and Wunsch* [1982] studied the trapping of baroclinic energy along a canyon and demonstrated that the internal wave energy was intensified at the head and near the floor of Hudson Canyon. One of the most prominent multidisciplinary canyon studies was conducted in Monterey Bay off the California coast. *Kunze et al.* [2002] indicated that the internal gravity waves in Monterey Canyon are an order of magnitude more energetic than those in the open ocean. The tidal-period-averaged, vertically integrated baroclinic energy flux is O(5 kW m^{-1}) in the canyon [*Kunze et al.*, 2002]. For comparison, the baroclinic energy flux is O(10–20 kW m^{-1}) in energetic baroclinic tidal regions, such as the Hawaiian Ridge [*Rudnick et al.*, 2003] and the Luzon Strait [*Duda et al.*, 2004; *Jan et al.*, 2008]. The baroclinic tidal energy in Monterey Canyon lies between those on abrupt topographic ridges and in the open ocean. In addition to the research of *Kunze et al.* [2002], *Jachec et al.* [2006] estimated that 52 MW of net baroclinic tidal energy propagates to the open ocean, and 8.3 MW is dissipated locally. *Hall and Carter* [2011] constructed a similar energy budget for Monterey Canyon using the Princeton Ocean Model (POM) and presented a thorough discussion on both the observational and the model results.

[3] Compared to Monterey Canyon, the Gaoping Submarine Canyon (GPSC; see Figure 1), which extends southwestward from the southwestern coast of Taiwan, is also a narrow, steep canyon with a similar spatial scale to that of Monterey Canyon. The width of the GPSC ranges from 1 km at its head to 8 km at its opening; the mean bottom slope is

[1] Institute of Oceanography, National Taiwan University, Taipei, Taiwan.
[2] Applied Physics Laboratory, University of Washington, Seattle, Washington, USA.
[3] Institute of Hydrological and Oceanic Sciences, National Central University, Jungli, Taiwan.

Copyright 2011 by the American Geophysical Union.
0148-0227/11/2011JC007366

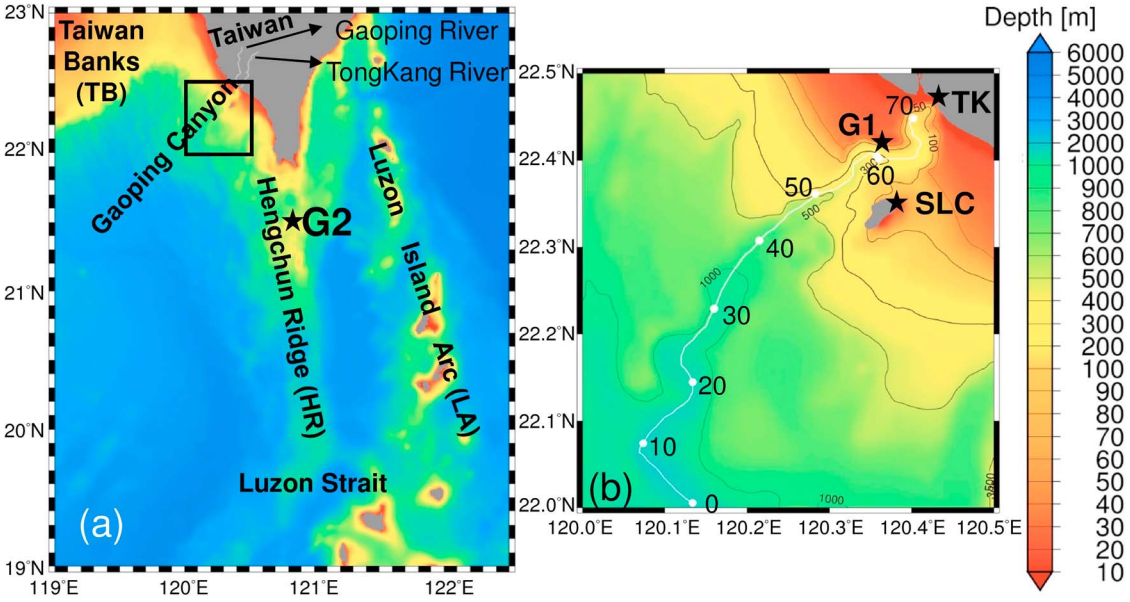

Figure 1. (a) Bathymetry chart for the sea around southern Taiwan. HR, LA and TB hereafter denote the Hengchun Ridge, Luzon Island Arc and the Taiwan Banks, respectively, in the figures. (b) A closer view of the topography in the Gaoping Canyon and vicinity indicated by the rectangle in Figure 1a. TK and SLC stand for the tide-gauge stations at Tong-Kang and Siao-Liou-Ciou, respectively. The white line indicates the thalweg of the GPSC. G1 is an anchor station for the shipboard CTD and LADCP measurements. The isobaths are in m; the bold numbers are in km.

approximately 0.03. Geographically, the GPSC is close to the Luzon Strait, which, along with the Luzon Island Arc and the Hengchun Ridge (Figure 1a), is one of the primary internal tide generating sites in the world oceans [*Lynch et al.*, 2004; *Ramp et al.*, 2004]. The GPSC connects the estuary of the Gaoping and Donggang Rivers to the deep northern South China Sea and is of importance in many aspects. Geologically, 36 million metric tons of suspended sediment is discharged from the Gaoping River to the sea each year, which is the second largest sediment discharge from a Taiwanese river [*Liu et al.*, 2002]. The sediment may be partially deposited in the canyon and partially delivered to the deep basin through the canyon. *Liu et al.* [2009] studied the behavior of a pronounced benthic nepheloid layer in the canyon and concluded that the concentration and thickness of the benthic nepheloid layer are closely related to the up-canyon flow of cold water from offshore. The authors suggested that the cross-canyon geometry and the bottom slope control the propagation of the barotropic and baroclinic tides in the canyon that, in turn, affect the generation of the benthic nepheloid layer. That is, the enhancement of the vertical mixing rate due to the energetic internal tides may be the cause of the re-suspension of sediments that forms the benthic nepheloid layer.

[4] Biologically, the GPSC is an important fishing ground for the highly valued sergestid shrimp (also called sakura shrimp) [*Chiou et al.*, 2000, 2003; *Wang et al.*, 2008]. The habitat of the shrimp is presumably affected by the physical environment, which is characterized by the vigorous baroclinic tides/waves in the canyon. Conceivably, the nonlinear internal tidal surges at the canyon head transport cold, nutrient-rich subsurface water to the surface layer near the canyon head [*Wang and Chern*, 1996]. Therefore, the growth of plankton and, in turn, the shrimp may benefit from the coupling of physical and biological processes.

[5] Physically, it is well-known that the internal motions in the GPSC are energetic. Based on direct current and hydrographic measurements, *Wang et al.* [2008] and *Lee et al.* [2009a, 2009b] depicted that the velocity amplitudes increased with the depth and proximity to the canyon head. Additionally, the cold bottom water moved up-canyon during floods, and warm water drained out of the canyon during ebbs. The inverse S-shaped GPSC is comparable to Monterey Canyon in spatial scale [*Lee et al.*, 2009a]; the depth-integrated baroclinic tidal energy, which peaked at approximately 14 kW m^{-1} at a particular spot in the GPSC [*Lee et al.*, 2009a], is greater than that of Monterey Canyon, which is 5 kW m^{-1} at the mouth and 1 kW m^{-1} at the head [*Kunze et al.*, 2002].

[6] In addition to intensive observations that may benefit from *Wang et al.* [2008], *Liu et al.* [2009] and *Lee et al.* [2009a, 2009b], a modest conductivity-temperature-depth (CTD) and lowered acoustic Doppler current profiler (LADCP) observational program was conducted onboard the R/V *Ocean Researcher*-I at anchor station G1 (120.334°E, 22.413°N; see Figure 1b) near the head of the GPSC during 4–5 September, 2010. The depth at G1 is 320 m, and the CTD and LADCP were profiled down to 250 m, which is 78% of the entire water column. The observations were conducted during a neap tide. To provide an essential feature of the internal wave-induced temperature fluctuation, Figure 2 illustrates the hourly sea levels, temperature and current velocity within a 25-h period at G1. The light transmission acquired during each CTD cast is also shown in Figure 2c and will be described in Section 4.4. The isotherm elevation at the main thermocline peaked at approximately low

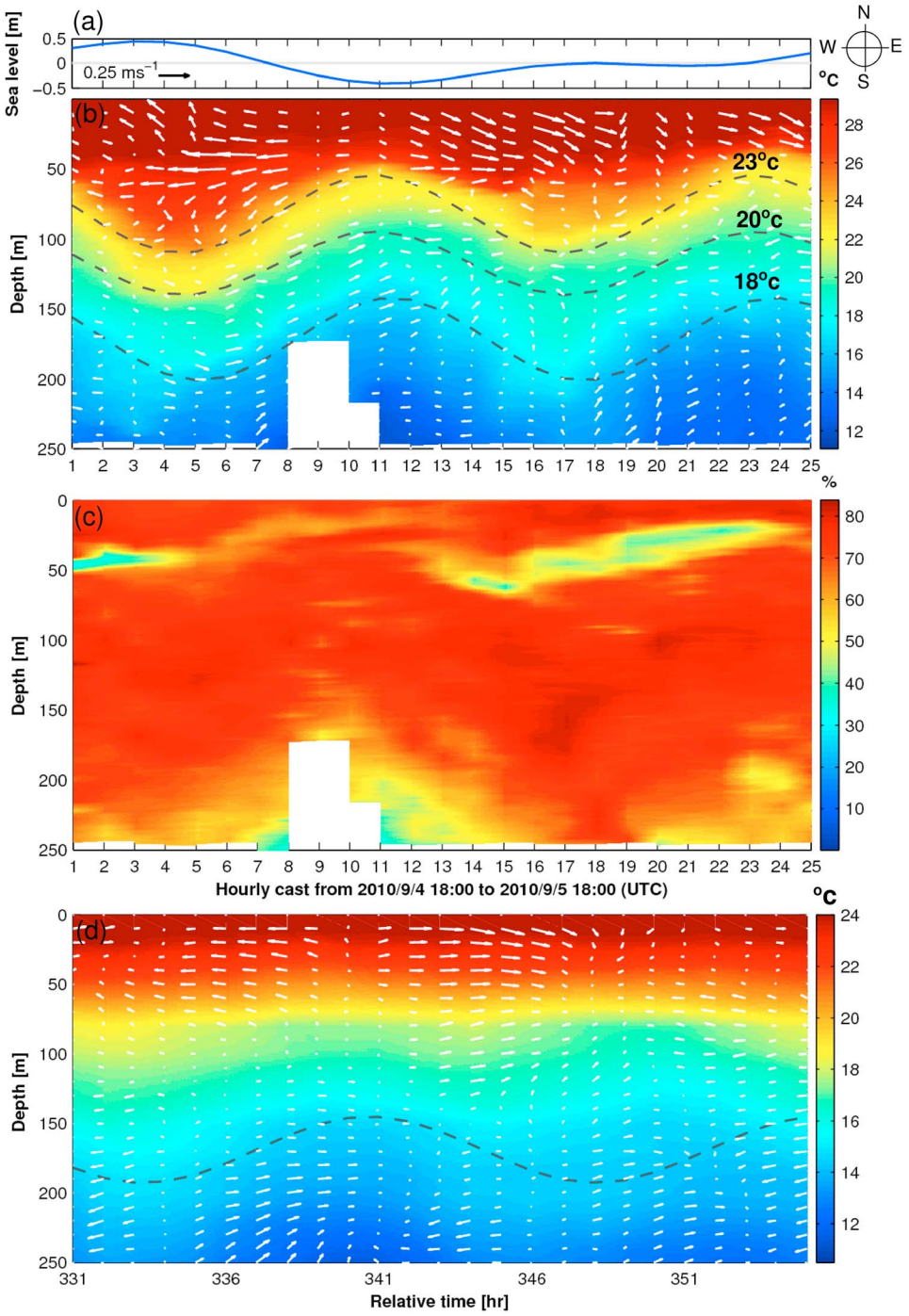

Figure 2. (a) Observed hourly sea level and time versus depth variation of (b) temperature and current velocity (c) light transmission (in %) from 4 September, 2010 at 18:00 to 5 September, 2010 at 18:00 UTC at G1. The dashed lines indicate the M_2 tide-fitted isotherm fluctuations for 23°C, 20°C and 18°C. (d) The model-produced hourly temperature profile and velocity at G1 within the 25-h period. The dashed line indicates the M_2 tide fitted 16°C isotherm fluctuation.

tide and reached the lowest level near high tide approximately 180° off-phase, thereby suggesting the strong effect of internal tides on temperature fluctuations over barotropic tides. The M_2 isotherm displacements at 23°C, 20°C and 18°C were approximately 50 m as computed using the least squared method described by *Isobe et al.* [2007]. In the surface mixed layer (approximately the upper 30 m), which is defined as the temperature vertical gradient $\partial T/\partial z <$ 0.05°C m^{-1}, the raw current velocity was approximately 0.25 m s^{-1} oscillating approximately along the coast, i.e., perpendicular to the local thalweg of the canyon. In a deeper layer near 200 m, the current velocity was approximately

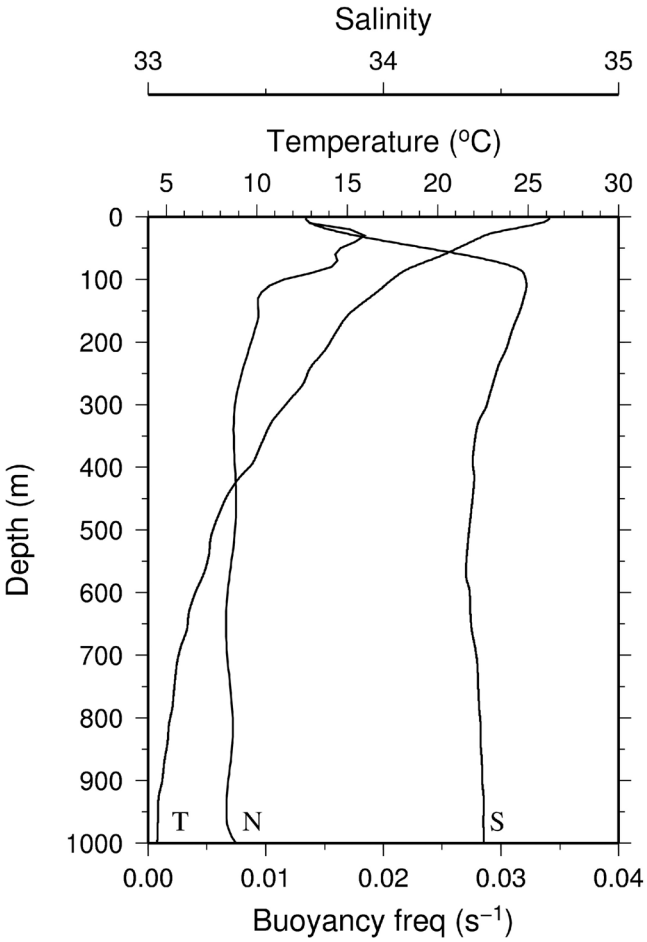

Figure 3. Temperature (T), salinity (S) and associated buoyancy frequency (N) profiles compiled from historical CTD data around the GPSC for the initial field of a model run.

0.2 m s^{-1}, and its major axis was aligned roughly along the canyon, i.e., northeast-southwestward. The major axis of the M_2 fitted baroclinic tidal current ellipse was parallel to the coast with a semi-major axis of approximately 0.1–0.2 m s^{-1} in the surface layer but was turned to follow the canyon and a semi-major axis of 0.2 m s^{-1} in the deeper layer (not shown). The 25-h time-mean, depth-integrated baroclinic tidal energy flux was 2.5 kW m^{-1} at station G1, which was estimated using the observed hydrography and current velocity. Note that the estimate did not cover the missing data near the surface and in depths below 250 m. The detailed properties of the observed internal tides in the GPSC are summarized by *Lee et al.* [2009a]. To facilitate data analysis, sea level data at two coastal tide gauge stations, specifically, Tong-Kang (TK in Figure 1b) and Siao-Liou-Ciou (SLC in Figure 1b), were collected.

[7] The purpose of this study is to understand the dynamics of baroclinic tides and to quantify their energetics in the GPSC. Particular interest is focused on the source of baroclinic tidal energy and the mechanism for the intensification of baroclinic tides in the GPSC. A three-dimensional model was adopted for this study. Harmonic constant-composed tidal sea levels at the open boundaries were used to drive the model. The model configuration and corresponding validation of simulated tides are described in section 2. The characteristics and energetics of the simulated barotropic and baroclinic tides off and in the GPSC are delineated in section 3. Section 4 discusses and evaluates the energy source for the baroclinic tides in the GPSC. In order to quantify whether the baroclinic energy generated in the Luzon Strait or the southeastern Taiwan Strait is crucial to baroclinic tides in the GPSC, a "baroclinic filter," which, as described in section 4.2, utilizes the flow relaxation scheme rather than an increase in viscosity, is applied to diminish the baroclinic tidal energy in the aforementioned generation regions. Potential mechanisms for partial standing internal tides off the GPSC and near-resonance internal tides in the GPSC are discussed in section 4.3. The conclusions are stated in section 5.

2. Model Configuration and Validation

[8] A three-dimensional, hydrostatic, primitive equation model, POM [*Blumberg and Mellor*, 1987], was adopted to simulate barotropic and baroclinic tides and to examine sources of baroclinic tides in the GPSC. The vertical axis of the model was transformed to the σ−coordinate by $\sigma = (z - \eta)/(H + \eta)$, where z is the positive upward with the origin placed at the mean sea level, η is the sea level fluctuation and H is the mean water depth. The governing equations are described by *Blumberg and Mellor* [1987] and, for the sake of brevity, are not shown here. An artificial damping term was added to the horizontal momentum equation to represent the momentum dissipation and conversion to unresolved non-hydrostatic processes and nonlinear internal waves. The damping term is defined as $-r(\vec{u} - \langle\vec{u}\rangle)$, where $\vec{u}$ is the horizontal velocity vector in Cartesian coordinates, $\langle\rangle$ represents the depth average and r is a damping coefficient. We used $r = 0.2$ day^{-1}, which is used by *Niwa and Hibiya* [2004]. The tidal potential was neglected in this simulation because the model domain was smaller than a typical wavelength of a semidiurnal barotropic tide in this region. POM uses the hydrostatic approximation and can resolve weakly nonlinear internal tides that neglect non-hydrostatic dispersion [*Jan and Chen*, 2009], which is adequate for the purpose of this study.

[9] To examine better the source of baroclinic energy in the GPSC, the computational domain covered the Luzon Strait and the continental shelf near the Taiwan Banks (see Figure 1a). The computational domain was bounded from 119.0°–122.5°E and 19.0°–23.0°N (the inset in Figure 1a), with horizontal resolution that varied from 500 m in and around the GPSC to 2000 m elsewhere. There were 31 uneven σ layers, which were finer in the surface and bottom layers. The transformed non-dimensional depth for each layer was 0, 0.00068, 0.00136, 0.00204, 0.00339, 0.00611, 0.01154, 0.02240, 0.04413, 0.08758, 0.13103, 0.17447, 0.21792, 0.26137, 0.30482, 0.34827, 0.39172, 0.43517, 0.4786, 0.52206, 0.56551, 0.60896, 0.65241, 0.69586, 0.73931, 0.78276, 0.82621, 0.86965, 0.91310, 0.95655 and 1 from the surface to the bottom. The model topography was constructed by a 500-m grid resolution bathymetric data set from the Ocean Data Bank (ODB) of the National Science Council of Taiwan.

[10] Figure 3 shows the initial mean temperature (T), salinity (S) and associated buoyancy frequency (N) profiles

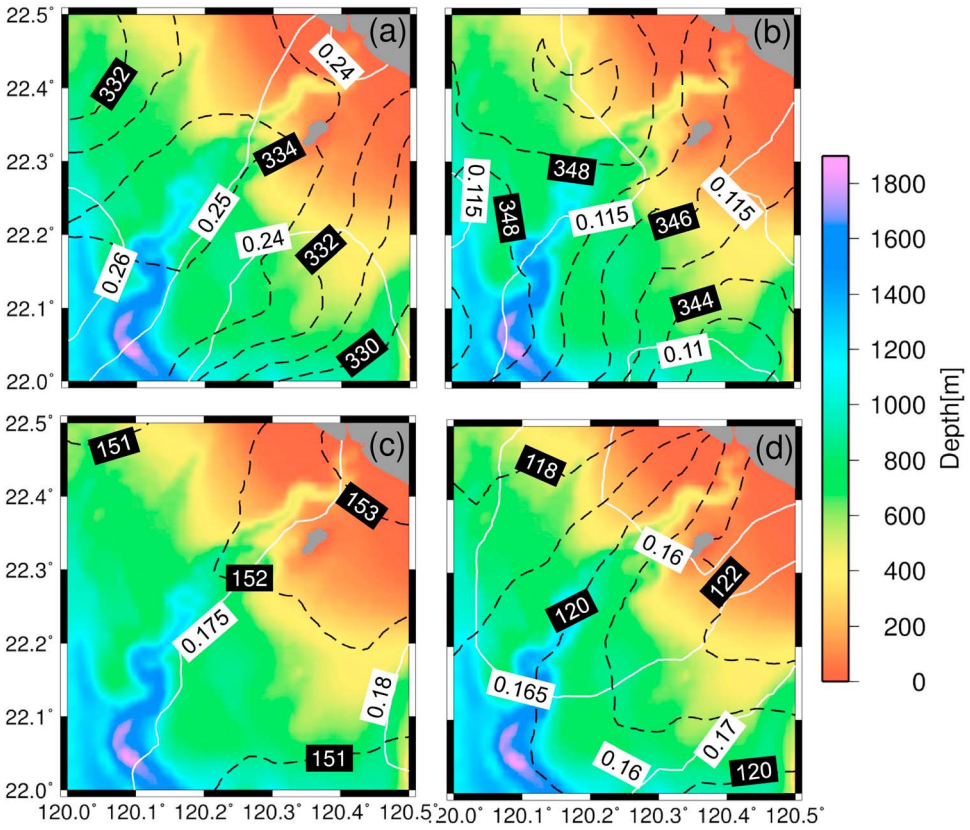

Figure 4. Co-tidal charts derived from model-simulated (a) M_2, (b) S_2, (c) K_1 and (d) O_1 tides in the GPSC and vicinity. The black dashed lines are phases in degrees (referred to the Greenwich Mean Time); the white lines are amplitudes in meters.

for depths above 1000 m, which were obtained by averaging historical CTD data collected in 119.5–120°E and 21.5–22°N. Below 1000 m, the vertical profiles of T, S and *N* show no significant depth and seasonal variation; therefore, both the T and S were set as constants with their 1000 m values. The initial T and S fields were horizontally homogeneous to exclude the thermal wind currents. The ocean model was motionless initially and was subsequently driven by the prescribed tidal sea levels on all of the open-ocean boundaries through a forced radiation condition similar to that used by *Blumberg and Kantha* [1985]. The tidal sea levels on the open boundaries were composed using harmonic constants (M_2, S_2, K_1 and O_1) that had been compiled in a database TWTIDE08 [*Hu et al.*, 2010]. The horizontal viscosity and diffusivity were computed according to the formula described by *Smagorinsky* [1963]. The vertical viscosity and diffusivity were determined by a level 2.5 turbulence-closure scheme [*Mellor and Yamada*, 1982]. A quadratic stress law was applied as the bottom boundary condition. A model run, driven by four principal tidal constituents (M_2, S_2, O_1 and K_1), was 35 days long. Hourly model results after Day 5, when the simulation reached a cyclic equilibrium in kinetic energy, were stored for analysis. Importantly, the error caused by the computation of the horizontal pressure gradient in POM commonly causes unwanted low-frequency velocities [*Haney*, 1991; *Mellor et al.* 1994]. However, these erroneous velocities could effectively be removed using harmonic analysis and canceled out during depth integration [*Hall and Carter*, 2011].

[11] The harmonic constants calculated from the simulated barotropic tides were compared with those from observations described in the literature. Figure 4 shows the co-tidal charts of the simulated O_1, K_1, M_2 and S_2 tides around the GPSC. The amplitude of M_2 ranges between 0.23 and 0.25 m. The amplitude of both O_1 and K_1 is 0.15–0.17 m. The amplitude of S_2, approximately 0.11 m, is smaller than that of the other three constituents. The spatial variations of tidal phases indicate that the tidal waves propagate northwestward along the coast. Both the co-amplitude and co-phase of the simulated tides are essentially consistent with those shown in previous studies [e.g., *Lefèvre et al.*, 2000; *Matsumoto et al.*, 2000] but with discrepancies mainly sourced from the baroclinic modulation of barotropic tides. Similar modulation can be seen from simulated barotropic tides in and around the Luzon Strait [*Jan et al.*, 2007] and in Monterey Bay [*Carter*, 2010]. The amplitude and phase for M_2, S_2, O_1 and K_1, which are calculated from observed sea level data, respectively, are (0.218 m, 329°), (0.082 m, 351°), (0.154 m, 121°) and (0.158 m, 153°) at TK and (0.227 m, 335°), (0.093 m, 348°), (0.159 m, 121°) and (0.165 m, 151°) at SLC. The root-mean squared (RMS) difference of the simulated tidal sea level is 0.03 m at TK and SLC. The depth-averaged tidal current ellipses in Figure 5 show that the major axes are essentially parallel to the coastline (northwest-southeast)

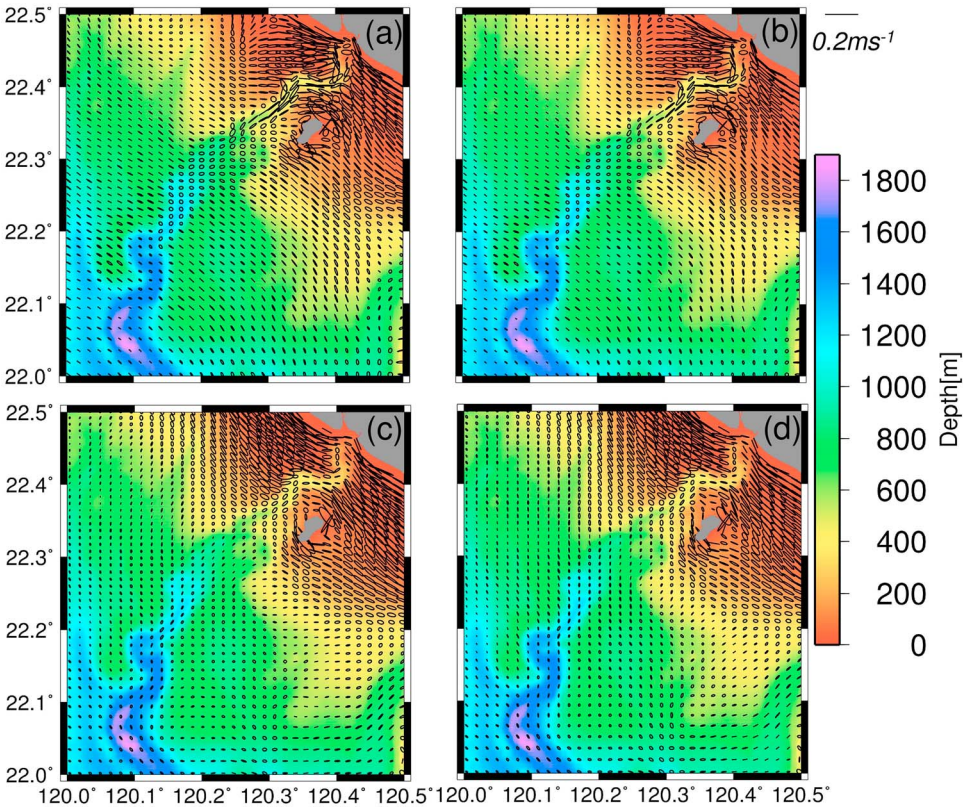

Figure 5. Depth-averaged tidal current ellipses derived from model-simulated (a) M_2, (b) S_2, (c) K_1 and (d) O_1 tides in the GPSC and vicinity.

near the coast but turn to align with the thalweg of the GPSC. The velocity amplitudes are 0.2, 0.1, 0.15 and 0.15 m s^{-1} for M_2, S_2, O_1 and K_1, respectively, around the GPSC.

[12] Figure 2d illustrates the model-produced hourly temperature profile and velocity at G1. Compared with Figure 2b, the vertical fluctuation in the modeled temperature field is similar to that of the observed temperature; the vertical displacement of M_2 tide-fitted 16°C isotherm (dashed line in Figure 2d), approximately 40 m, agrees with the vertical displacement of the 18°C isotherm in Figure 2b. The vertical structure of the modeled velocities is consistent with the raw data shown in Figure 2b. The modeled tidal currents with a maximum speed of approximately 0.2 m s^{-1} oscillate northwestward and southeastward in the mixed layer but in nearly perpendicular directions in near bottom layers to those in the surface layers. The weakest modeled currents occur in the middle layer, which is similar to that demonstrated in Figure 2b. The modeled temperature and current velocity reasonably agree with the observations with the RMS difference ranging between 62% and 185%, suggesting that the model's results are adequate for performing further analyses on the modeled baroclinic tides in the GPSC. Nonetheless, the discrepancy between the modeled fields and the observations, although minor, can be seen between Figures 2b and 2d. The discrepancy could be caused by the limited constituents in tidal forcing, the simplified initial conditions, and the truncation error in model topography due to the horizontal grid resolution. The corresponding sensitivity tests for these parameters are out of the scope of this study but merit a future study.

3. Barotropic and Baroclinic Tides in the GPSC

[13] Figure 6 illustrates snapshots of the isopycnal vertical displacement relative to 150 m depth and the corresponding current velocities extracted from the results on Days 8, 8.25, 8.5 and 8.75. The estimate of the isopycnal vertical displacement $\xi(z, t)$ follows the procedure described by *Alford et al.* [2006]. The procedure takes the relative depth of each isopycnal in the initial density field $z(\rho_i)$ as a reference and computes the vertical displacement of each isopycnal relative to $z(\rho_i)$ as $\xi(z, t) = z(\rho, t) - z(\rho_i)$ for $\rho = \rho_i$. The pattern of displacement is consistent with that demonstrated in model results from *Niwa and Hibiya* [2004] and from *Jan and Chen* [2009]. The overall vertical displacement is approximately 40 m and can be greater than 60 m in the Luzon Strait (Figures 6b and 6c). The temporal variation of the vertical displacement in Figure 6 suggests that baroclinic tides generated in the Hengchun Ridge seemingly propagate eastward and northwestward to the Taiwan Banks. The wavelength of baroclinic tides comprised of the four tidal constituents is approximately 70 km at 150 m depth northwest of the Luzon Strait. The phase speed is approximately 1.6 m s^{-1}. The associated tidal currents demonstrate complicated patterns because the generation area occupies one third of the model domain. The flow field, a blend of barotropic and baroclinic tidal currents, varies dramatically in

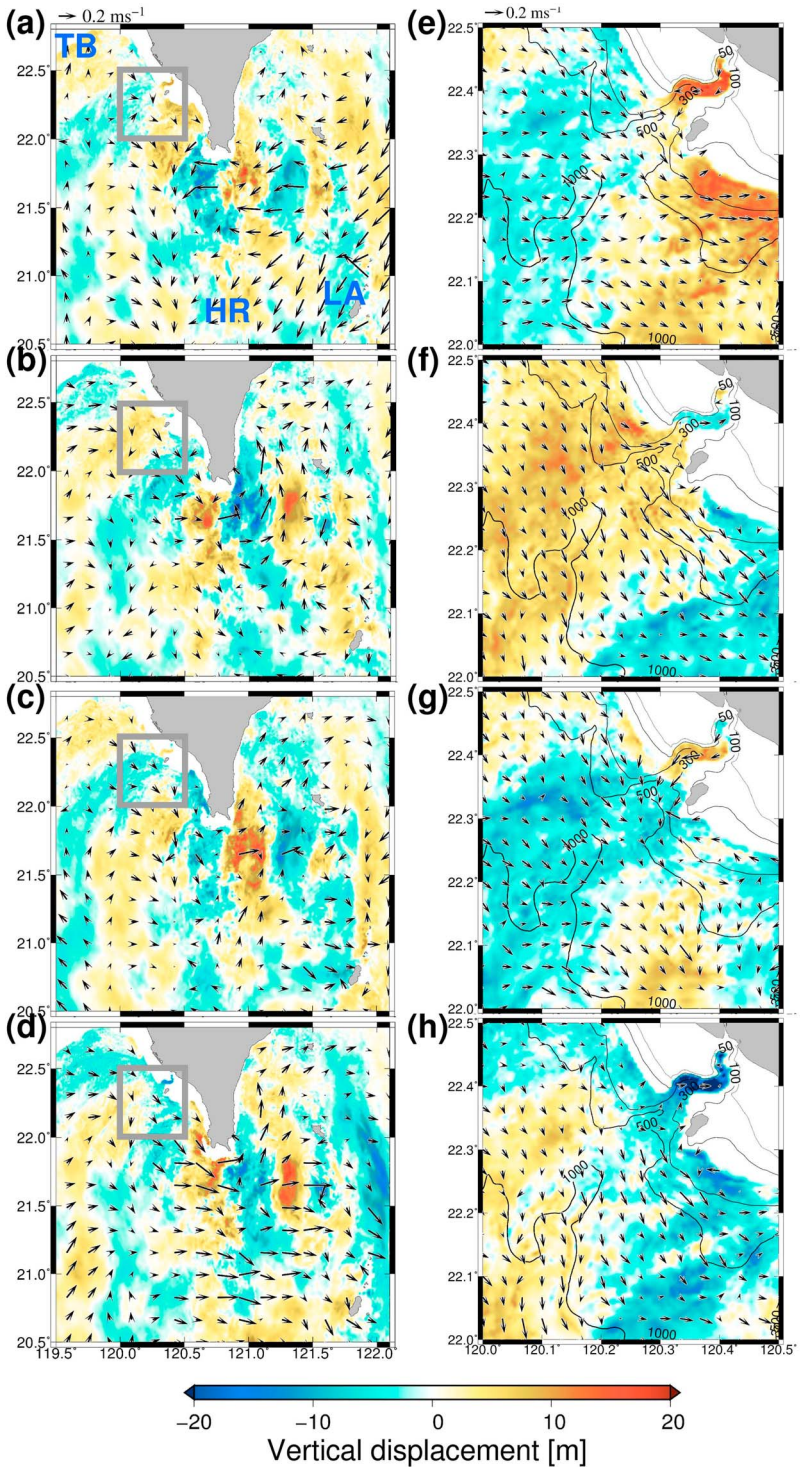

Figure 6. The instantaneous isopycnal vertical displacement relative to 150 m depth and the corresponding current velocities extracted from the results on Days (a) 8, (b) 8.25, (c) 8.5 and (d) 8.75. (e–h) Closer views of Figures 6a–6d, respectively, for those variables in the GPSC and vicinity.

space and time at the forced stage of baroclinic tide generation. Figures 6e–6h focus in on the GPSC and its vicinity and show that the vertical displacements increase with distance from the opening toward the head of the GPSC. The displacements remain greater than 40 m at depths of less than 200 m in the canyon.

[14] Figure 7 shows the instantaneous isopycnal vertical displacements of the simulated baroclinic tides at a section along the thalweg of the GPSC (white line in Figure 1b) on Days 8, 8.25, 8.5 and 8.75. The displacement of approximately 40 m is close to the observations reported in this study and by *Lee et al.* [2009a] and *Wang et al.* [2008]. The

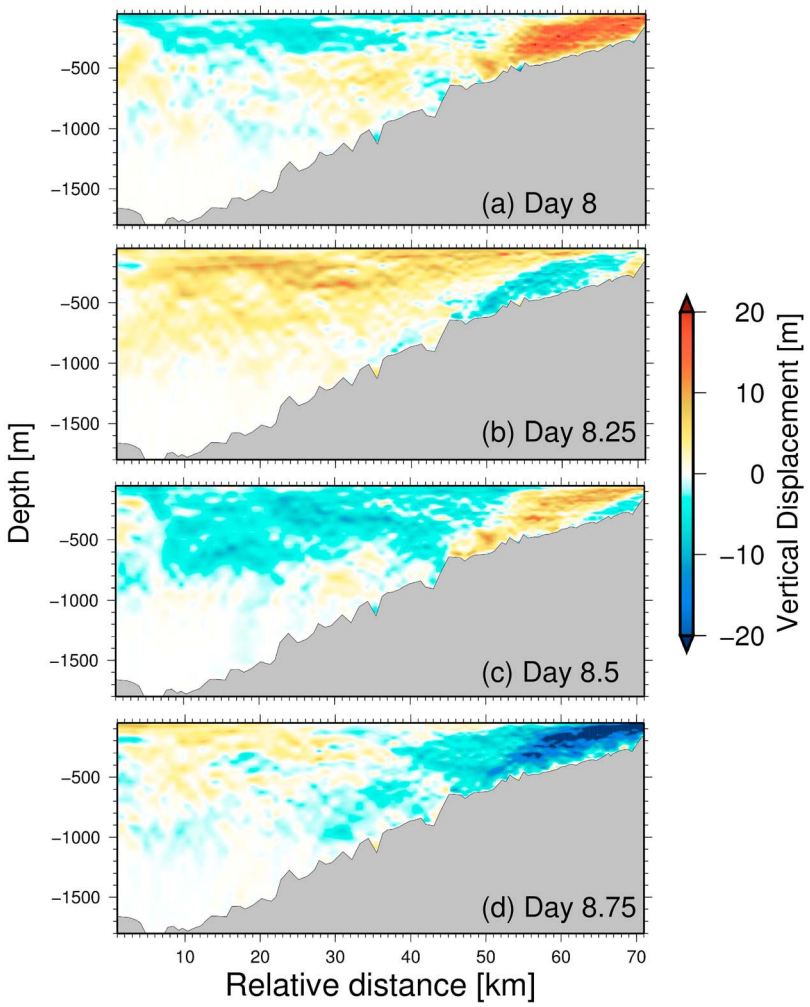

Figure 7. The instantaneous isopycnal vertical displacements of simulated baroclinic tides at a section along the major axis of the GPSC (white line in Figure 1b) on Days (a) 8, (b) 8.25, (c) 8.5 and (d) 8.75.

oscillation of the displacement is out of phase horizontally between the canyon head and the region approximately 20 km from the head and vertically at depths of 400–500 m in the canyon regions that are approximately 40 km from the head. The existence of horizontal and vertical nodes indicates a complicated dynamic of baroclinic tides in the GPSC.

[15] The energy of barotropic and baroclinic tides is often a measure of the wave propagation and dynamics. According to *Kunze et al.* [2002] and *Jan et al.* [2008], the depth-integrated barotropic (F_{bt}) and baroclinic (F_{bc}) energy fluxes averaged over 25-h are respectively calculated by the following equations:

$$F_{bt} = \frac{1}{T_{av}} \int_0^{T_{av}} \left(\langle \vec{u} \rangle \int_{-H}^{\eta} (g\rho_0 \eta + p') dz \right) dt \tag{1}$$

and

$$F_{bc} = \frac{1}{T_{av}} \int_0^{T_{av}} \left(\int_{-H}^{\eta} \vec{u}' p' dz \right) dt, \tag{2}$$

where ρ_0 represents the initial density stratification, g is the gravitational acceleration, $\vec{u}'$ is the baroclinic velocity vector in Cartesian coordinates, p' is the perturbation pressure, T_{av} (=25-h) is the average period and the angle brackets represent the depth average. The perturbation pressure is calculated by *Carter et al.* [2008] using the following equation:

$$p'(z) = \int_z^0 N^2 \zeta dz' - \left(\frac{1}{H} \right) \int_{-H}^0 \int_z^0 N^2 \zeta dz' dz, \tag{3}$$

where ζ is the isopycnal displacement. Figure 8 illustrates F_{bt} during spring and neap tide. Regardless of the fortnightly cycle, Figure 8 suggests that the barotropic tides, with F_{bt} ranging between 100 and 200 kW m^{-1}, propagate southwestward from the Pacific Ocean and pass through the Luzon Strait. Most of the barotropic energy that enters the South China Sea propagates westward. A fraction of the barotropic energy refracts around the southern tip of Taiwan to the deep channel in the southeastern Taiwan Strait. F_{bt} decreases to 50–80 kW m^{-1} after passing through the Luzon Strait, suggesting that a sizable amount of barotropic energy is dissipated or converted into another form of energy in the

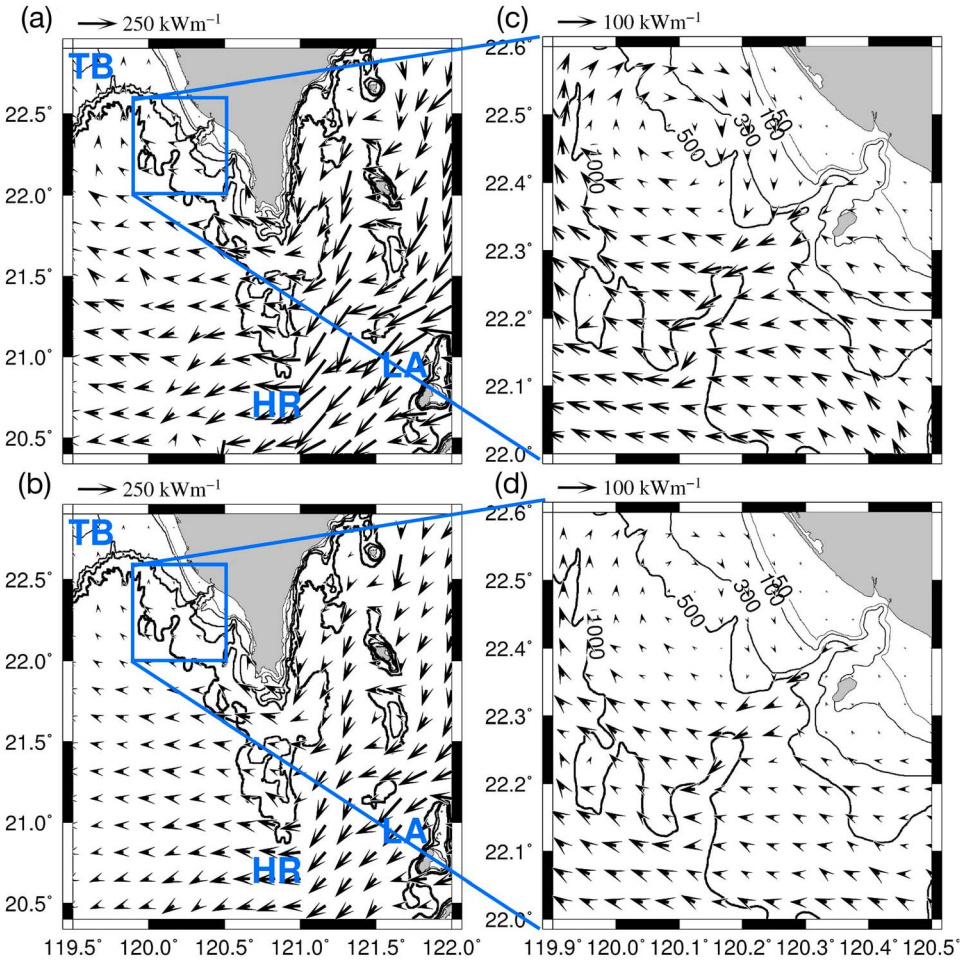

Figure 8. The barotropic energy flux averaged over 25-h during (a) spring and (b) neap tides. (c and d) Closer views of the region bounded by the blue rectangle in Figures 8a and 8b. The 50, 100, 300, 500 and 1000 m isobaths are overlaid on each.

Luzon Strait. F_{bt} during neap tide is approximately two thirds of that observed during spring tide. Figures 8c and 8d show a close-up of F_{bt} distribution in the rectangle marked on Figures 8a and 8b. As the northwestward branch of F_{bt} reaches the GPSC, it turns southwestward and subsequently northwestward off the GPSC. F_{bt} directs outward from the canyon. The barotropic energy flux is approximately 10 kW m^{-1} near the canyon head and increases to approximately 20 kW m^{-1} at the canyon mouth and is 10–50% smaller in neap than in spring tides. The baroclinic energy flux is discussed in the next section.

4. Discussion

4.1. Sources of Baroclinic Energy in the GPSC

[16] The generation of baroclinic tides can be identified from the time mean, depth-integrated barotropic to baroclinic energy conversion rate (E_{bt2bc}), which is defined as follows [*Niwa and Hibiya*, 2004]:

$$E_{bt2bc} = \frac{1}{T_{av}} \int_0^{T_{av}} \left(g \int_{-H}^{\eta} \rho' w_{bt} dz \right) dt, \qquad (4)$$

where $w_{bt} = \langle \bar{u} \rangle (\sigma \frac{\partial D}{\partial x} + \frac{\partial \eta}{\partial x}) + \langle \bar{v} \rangle (\sigma \frac{\partial D}{\partial y} + \frac{\partial \eta}{\partial y}) + (\sigma \frac{\partial \eta}{\partial t} + \frac{\partial \eta}{\partial t})$ is the Cartesian vertical velocity relevant to the barotropic flow and ρ' is perturbation density. The energy conversion rate is averaged over 25-h during spring or neap tides. Figure 9 illustrates F_{bc} and E_{bt2bc} over the entire domain and a close-up for the two variables around the GPSC during spring and neap tides. E_{bt2bc} exhibits a similar pattern during spring and neap tides but at a different magnitude, which is similar to that described by *Holloway and Merrifield* [2003]. The baroclinic energy is primarily produced above both flanks of the Luzon Island Arc and the east flank of the Hengchun Ridge in the Luzon Strait. The generation site also comprises the southern slope of the Taiwan Banks, but its magnitude is weaker compared to that in the Luzon Strait. The propagation, fortnightly variation and magnitude of F_{bc} in the entire domain are consistent with the results given by *Niwa and Hibiya* [2004] and *Jan et al.* [2008]. In a broader view, the westward F_{bc} deflected from the Hengchun Ridge meets the southward F_{bc} reflected from the Taiwan Banks and, subsequently, both turn southward off southwestern Taiwan. The energy flux diminishes in this convergence zone because of the destructive interference. Part of F_{bc} turns northeastward

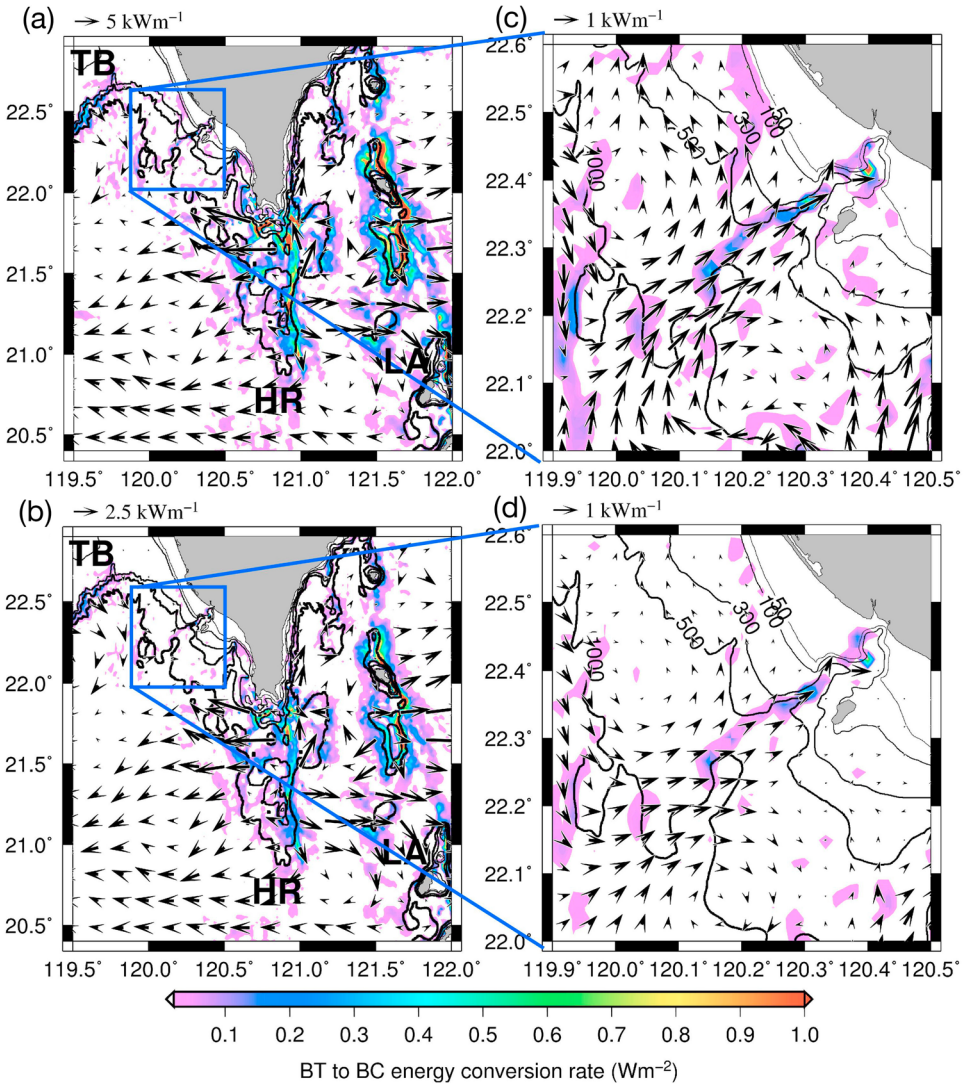

Figure 9. The time-mean (25-h), depth-integrated baroclinic energy flux (arrows) and depth-integrated barotropic-to-baroclinic energy conversion rate (colors) during (a) spring and (b) neap tides. (c and d) Closer views of the region bounded by the blue rectangle in Figures 9a and 9b. The 50, 100, 300, 500 and 1000 m isobaths are overlaid on each.

from the convergence zone. The dynamics of baroclinic tides in the GPSC and vicinity will be discussed later by means of a diagnostic for the partial standing wave that is described in the paper of *Martini et al.* [2007].

[17] Figures 9c and 9d show F_{bc} and E_{bt2bc} in and around the GPSC during spring and neap tides. F_{bc} is approximately 2 kW m^{-1} during spring tide and is reduced to less than 1 kW m^{-1} during neap tide. Importantly, the convergence of the northwestward- and southeastward-propagating F_{bc} outside the entrance of the GPSC probably causes a northeastward baroclinic tidal energy beam toward the canyon head. This feature suggests that the baroclinic tides generated outside the GPSC play a major role in supporting the baroclinic energy to the canyon. Figures 9c and 9d show that E_{bt2bc} in the GPSC is small with values of 0.1–0.3 W m^{-2}. Note that the F_{bc} of 14 kW m^{-1} estimated by *Lee et al.* [2009b] is greater than that estimated using both the observed and modeled data of this study. *Lee et al.* [2009b] computed the F_{bc} using the strongest current velocity data measured during a 28-h, hourly CTD and ADCP measurement. The authors stated that the estimate may not be representative as typical characteristics of the canyon. Indeed, the duration of 28-h for the time mean was not a tidal period or a multiple of the tidal period, which causes a certain bias in the estimated F_{bc}. The CTD was deployed down to a depth of 78% of the total water column, which causes additional bias in the estimated F_{bc}. Moreover, the observed current velocities from the other measurements at different locations described by *Lee et al.* [2009a] were much smaller than those used to compute the baroclinic energy flux by *Lee et al.* [2009b]. Therefore, the F_{bc} computed in this study is more reliable than that found by *Lee et al.* [2009b].

[18] The isopycnal vertical displacements increase with distance from the mouth to the head of the GPSC (Figures 6e–6h and 7), whereas the associated F_{bc} along the thalweg of the GPSC decreases toward the head of the GPSC. This

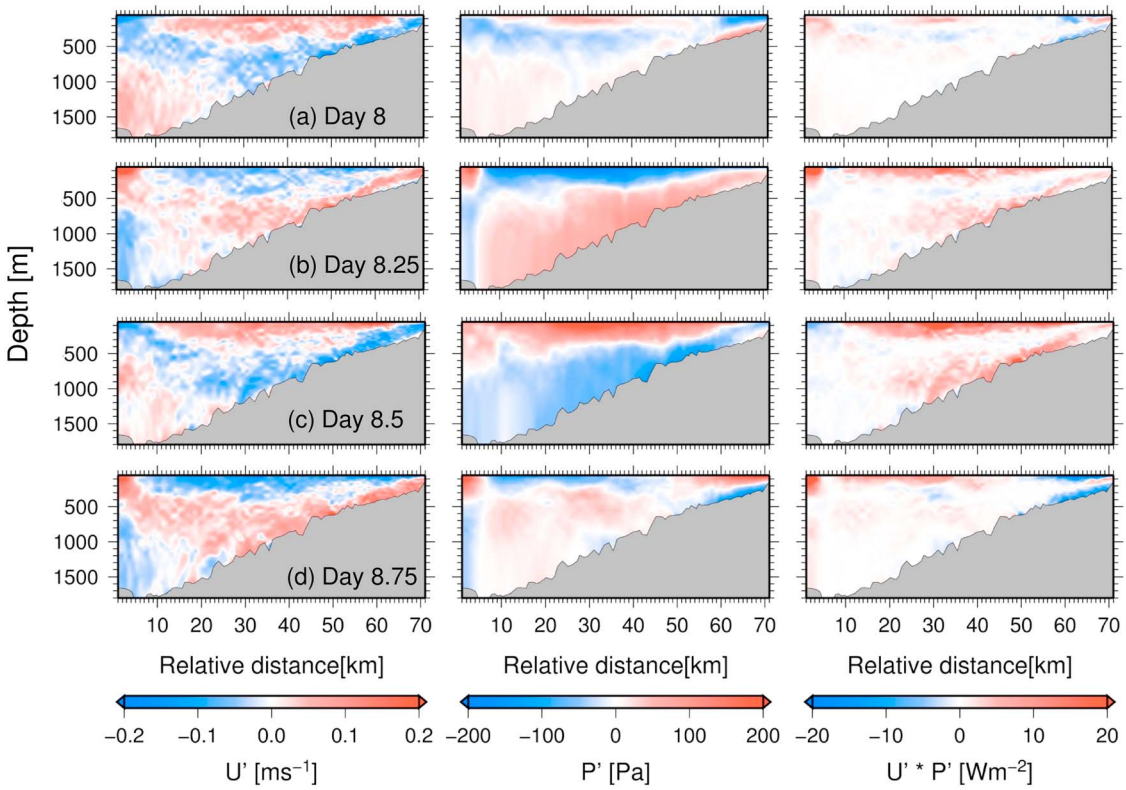

Figure 10. Vertical transects of the instantaneous zonal baroclinic velocity (u'), perturbation pressure (p') and zonal baroclinic energy flux ($u'p'$) along the GPSC axis on Days (a) 8, (b) 8.25, (c) 8.5 and (d) 8.75. Positive values indicate toward the canyon head.

pattern is indicative of a standing wave. Figure 10 shows the vertical distributions of the instantaneous zonal baroclinic velocity (u'), perturbation pressure (p') and zonal baroclinic energy flux ($u'p'$) along the GPSC (positive indicates toward the canyon head) on Days 8, 8.25, 8.5 and 8.75. The out-of-phase oscillations between u' and p' near the canyon head (between 60 and 70 km in Figure 10) are further indicative of a standing wave. Therefore, the instantaneous $u'p'$ is non-zero, but the tidal period mean of $u'p'$ is nearly zero at the canyon head. The variation of u' and p' is almost in phase in the GPSC mouth and vicinity (between 20 and 60 km in Figure 10), thereby leading to a positive F_{bc}. The patterns of u' and p' and $u'p'$ in Figure 10 are notably similar to the modeled results for Monterey Canyon given by *Hall and Carter* [2011].

[19] To evaluate further the source of baroclinic energy in the GPSC, the timing of the fortnightly cycle in the barotropic tidal level and in the 15°C isotherm vertical displacement at stations G1 and G2 (see Figure 1) were compared. The minimal (or maximal) tidal sea level difference and, therefore, a minimal (or maximal) barotropic tidal forcing during a fortnightly cycle occurs at neap (or spring) tide. At the baroclinic generating site, the isotherm displacement varies with the fortnightly variation of the tidal forcing. If F_{bc} is mainly generated in the GPSC, the minimal (or maximal) isotherm displacement is expected to occur simultaneously at neap (or spring) tide. If F_{bc} is generated at the canyon mouth, it requires approximately 4.5-h to travel from mouth to head, as estimated by the phase speed of approximately 1.2 m s^{-1} and a distance of 20 km. The time variation of tidal sea levels in Figure 11a suggests that the discrepancy in modeled barotropic tides at G1 and G2 is visibly indistinguishable. However, the vertical displacements of the 15°C isotherm at G1 and G2 in Figures 11b and 11c, respectively, differ in phase significantly. Comparing Figures 11e and 11f, the timing of the minimal 15°C isotherm displacement at the two stations has a 25-h difference. This finding indicates that the baroclinic tide at G1 lags behind that at G2 by 25-h, supporting that the baroclinic tidal energy in the GPSC is largely from the Luzon Strait. Given an estimated phase speed of baroclinic tides (1.6 m s^{-1}) and the distance between the mouth of the GPSC and G2 in the Luzon Strait (120 km), the northwestward-propagating baroclinic tides generated at G2 take 20.8-h to the canyon mouth and then take 4.5-h to G1, which is consistent with the time lag of 25-h deduced from Figures 11e and 11f.

4.2. Contribution of Local and Remote Baroclinic Energy Generation

[20] The potential sources of the baroclinic tides in the GPSC include the local generation within the canyon and remote generation at the two ridges in the Luzon Strait and the continental slope south of the Taiwan Banks. To quantify the contribution of each generation site, three additional numerical experiments were performed with the application of an artificial "baroclinic filter" zone over different "hot spots" of baroclinic tide generation. To exclude the baroclinic tide generation in a numerical model, a commonly adopted

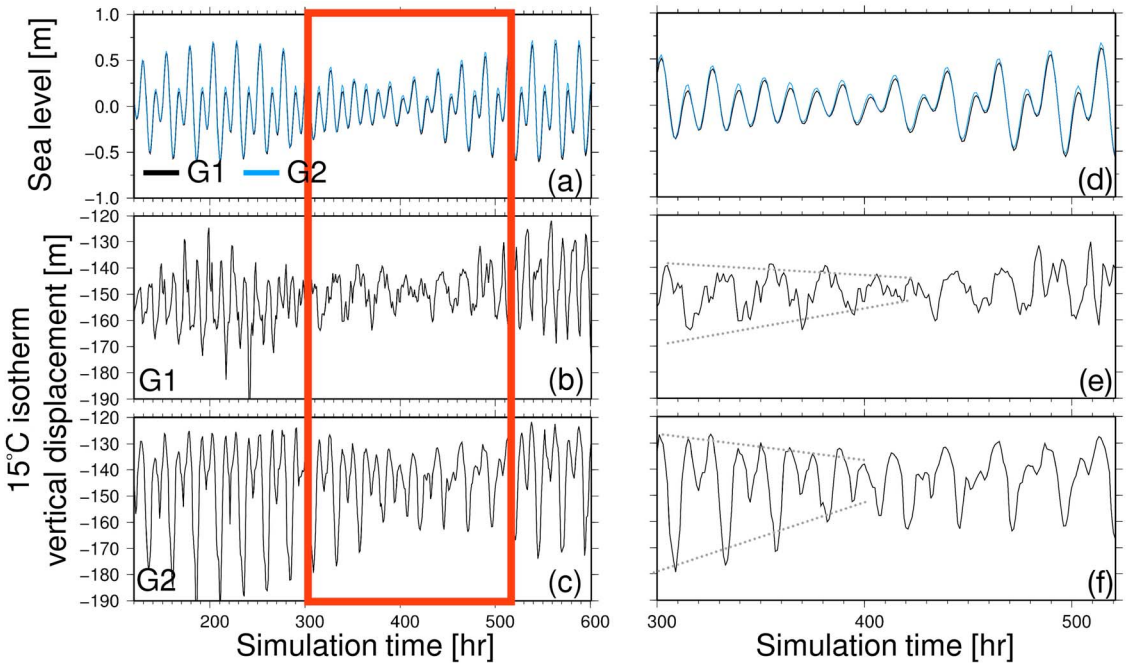

Figure 11. (a–c) Time series of simulated tidal sea levels and vertical displacements of the 15°C isotherm at Stations G1 and G2 (see Figure 1a for their locations). (d–f) Close-ups of Figures 11a–11c in the period bounded by red rectangular.

method is to reduce the ridge height of the topographic ridge, or even to remove the ridge from the model topography. However, the reduction of the ridge height or the removal of a ridge alters the bathymetry and thus changes the harmonics, i.e., the amplitude and phase, of the barotropic tides. To overcome the dilemma, the flow relaxation scheme, which is normally used as an open boundary condition, as described by *Martinsen and Engedahl* [1987], was used in the filter zone to remove the baroclinic component in the velocity and hydrographic fields but retain the barotropic characteristics. The 3-D velocity $\vec{u} = \vec{u}' + \langle\vec{u}\rangle$ and hydrography $\phi = (T' + T_i, S' + S_i)$ in the filter zone are forced to be as follows:

$$\vec{u} = \alpha\vec{u}' + (1-\alpha)\langle\vec{u}\rangle$$

and

$$\phi = \alpha\phi + (1-\alpha)\Phi,$$

where Φ represents the initial (T_i, S_i), and α is a coefficient that tends toward 1 in the center but to 0 at the outer edges of the filter. Briefly, with a change in α from 1 to 0 linearly in terms of the distance from the center to the outer edge of the filter, the baroclinic oscillation in hydrography and velocity diminishes from the center to the periphery of the filter zone, but the barotropic components remain unchanged. Table 1 lists the locale of the baroclinic filter in each experiment. The locale of the filter zone is shown by the shaded area in Figure 12. Each experiment run length was 12 days; the hourly variables from Day 6 were stored and are analyzed below.

[21] Figure 13 shows the vertically integrated F_{bc} and E_{bt2bc} averaged over seven days (from spring to neap tides) for the simulation from the three experiments and the control run. The spring-neap variation is eliminated. Without the baroclinic energy generation in both the Luzon Strait and the Taiwan Banks (Exp 3 in Figure 13d), the F_{bc} is greatly reduced in the GPSC area. The major discrepancy between F_{bc} in Exp 1 (Figure 13b) and Exp 2 (Figure 13c) and that in the control run (Figure 13a) is the lack of a northeastward baroclinic energy beam toward the canyon in Exp 1 and Exp 2. The vertical sectional-area integration of F_{bc} at the three sections bounded the GPSC (blue rectangle in Figure 13). The primary baroclinic influx from the mouth feeding into the canyon is 9.1 MW; baroclinic energy of a magnitude of 0.4 MW and 0.2 MW leaves the canyon through the northwest and southeast boundaries of the blue box. Without the remote baroclinic energy source from either the continental slope (Exp 1) or the Luzon Strait (Exp 2), the influx dramatically diminishes to 3.3 MW and 1.2 MW, respectively. The area-integrated E_{bt2bc} over the GPSC is 1.5 MW for the control run and is −0.9 MW, 0.7 MW and −0.2 MW, respectively, for Exp 1, Exp 2 and Exp 3. The changes in E_{bt2bc} are similar to those in Monterey Canyon [*Hall and Carter*, 2011] in that they are probably due to a pressure perturbation feedback between generation sites at the Luzon Strait and the Taiwan Banks. The vertically integrated F_{bc} at the mouth of the GPSC in the control run, 9.1 MW, is further

Table 1. Description of Numerical Experiment

Experiment	Locale of the Baroclinic Filter
1	Southern slope of Taiwan Banks
2	Hengchun Ridge
3	Both locales for Experiments 1 and 2

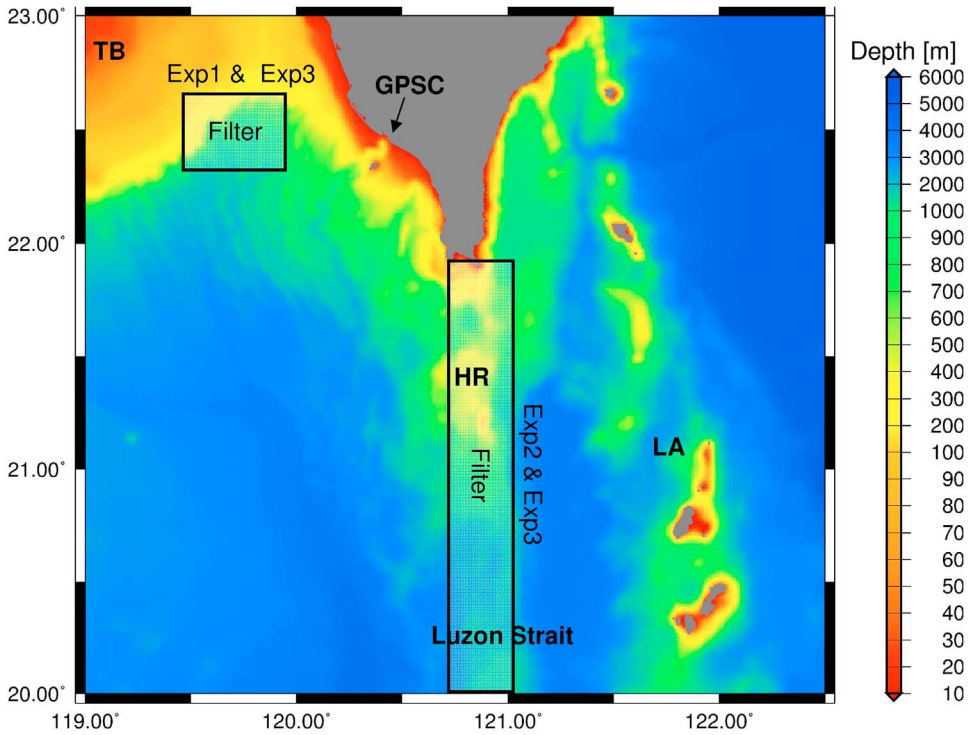

Figure 12. The locale of the baroclinic filter zone (shadow area) relative to the model domain.

taken as the total baroclinic energy fed into the canyon for estimating the contribution of the local generation and the generation in the Luzon Strait and the southern Taiwan Banks. The local generation is defined as the baroclinic energy generated by the oscillated local barotropic tidal current on the steep topography of the canyon. Without the input of baroclinic energy from the Luzon Strait and the southern Taiwan Banks, the vertically integrated F_{bc} in Exp 3 (Figure 13d) indicates that the local generation is only approximately 4.4% of the total baroclinic energy. Assuming that local generation accounts for 4.4% in all cases, 31.9% (from Exp 1 in Figure 13b) and 8.8% (from Exp 2 in Figure 13c) of the total baroclinic energy respectively emanate from the Hengchun Ridge and the southeast flank of the Taiwan Banks, which propagate directly into the canyon. The other 54.9% of the total baroclinic energy, which is not explained by Figure 13 but will be discussed in next section, may be related to the magnification of baroclinic energy, due to partial standing baroclinic tides outside and near the head of the GPSC.

4.3. Partial Standing Internal Waves Outside and in the GPSC

[22] Similar to a surface gravity standing wave, an internal standing wave could happen when two waves with the same amplitude and frequency propagate horizontally in opposite directions. *Alford et al.* [2006] and *Martini et al.* [2007] studied the observed and modeled results and verified the existence of a partial internal standing wave in Mamala Bay, Hawaii. The internal standing wave-related transverse baroclinic energy fluxes may enhance baroclinic tides in the bay.

[23] Transmitted baroclinic tides from the south and reflected baroclinic tides from the north meet each other off the southwestern coast of Taiwan. Similar partial standing baroclinic tides may occur off the mouth of the GPSC, causing the enhancement of baroclinic tidal energy in the GPSC. Following the analysis of Martini *et al.*, the time-averaged, depth-integrated horizontal kinetic energy (*HKE*), which is defined as $\rho_0(u'^2 + v'^2)/2$, and the available potential energy (*APE*), which is defined as $g^2\rho'^2/(2\rho_0 N^2)$, were calculated. The group velocity, which is defined as $C_g = F_{bc}/E$, where $E = HKE + APE$, was also estimated from the model-produced baroclinic tides. For progressive baroclinic tides, the *HKE*, *APE* and F_{bc} are approximately constants in space. For a purely internal standing wave, the maxima of *HKE* and *APE* occur alternately at a separation distance of a quarter-wavelength of the two opposite waves [*Nash et al.*, 2006; *Martini et al.*, 2007], i.e., at the node and the anti-node of the standing wave. The *HKE* and *APE* are equal at the middle between two adjacent *HKE* and *APE* maxima. Transverse energy flux is created at locations where $HKE \approx APE$ [*Nash et al.*, 2006]. A partial standing wave occurs when amplitudes of the two opposite incident baroclinic tides are unequal. The group speed, C_g, at the locations of maxima *HKE* and *APE* is normally smaller than that at locations of $HKE \approx APE$ for a standing wave [*Martini et al.*, 2007]. Figure 14 illustrates the time mean (seven days) depth-integrated *HKE* and *APE* ratio and the associated C_g for the control run. According to the diagnostic of a partial standing wave, one of the $HKE \approx APE$ locations aligns approximately in the direction of the thalweg of the GPSC. From this location, a transverse baroclinic energy beam propagates toward the canyon head. The spatial variation of C_g further supports the existence of the partial standing baroclinic tides. When either or both of the two incident baroclinic tides are excluded in Exp 1, Exp 2 or Exp 3, not surprisingly, the partial standing

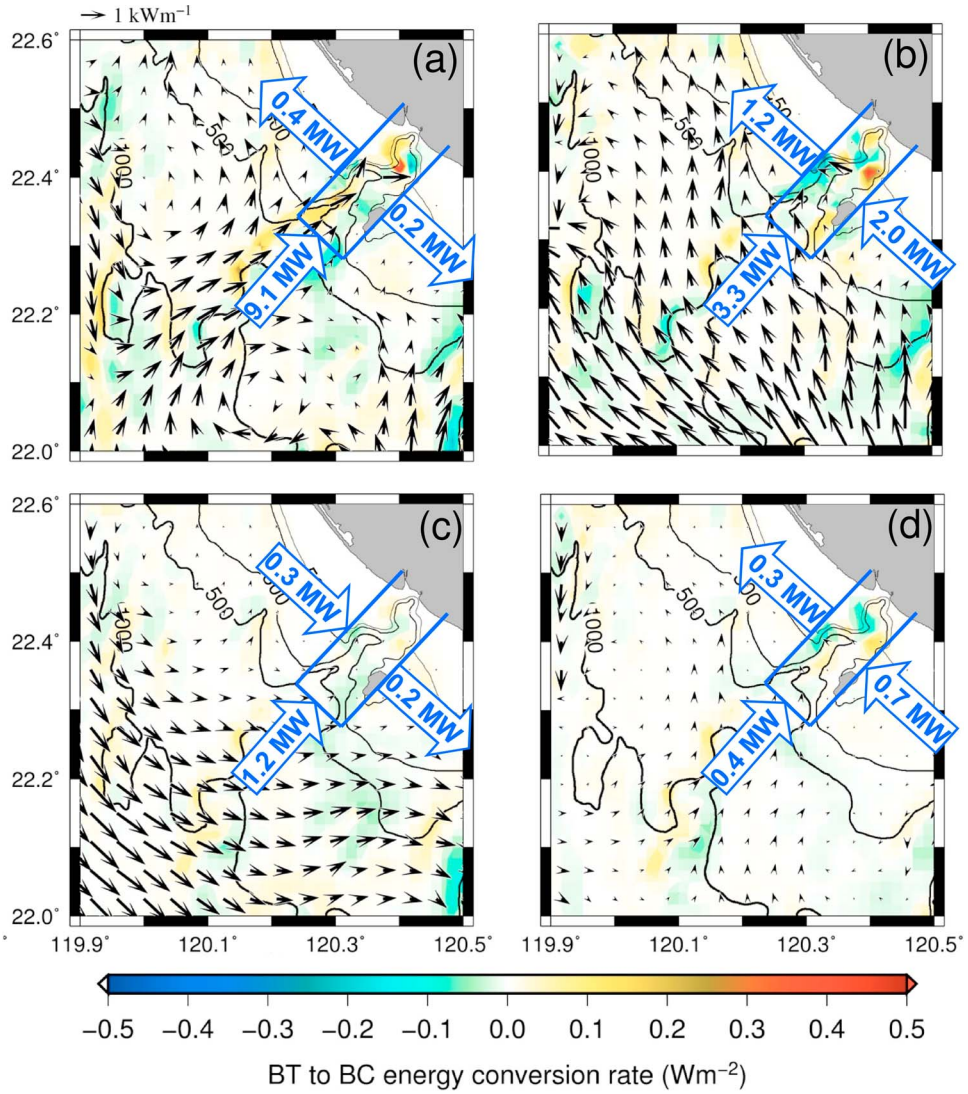

Figure 13. The vertically integrated F_{bc} (arrows) and E_{bt2bc} (colors) averaged over seven days of simulation from (a) the control run, (b) Exp1, (c) Exp2 and (d) Exp3. The blue rectangle enclosing the GPSC denotes the area for E_{bt2bc} and baroclinic energy integration. The blue open arrow and the number inside it indicate the sectional area-integrated F_{bc} in MW and the associated direction across the interface.

baroclinic tide off the GPSC vanishes. This result suggests that the energy flux radiating from both the Luzon Strait and the Taiwan Banks is vital to the formation of the standing waves off the GPSC.

[24] Two plausible mechanisms for the formation of internal standing tides outside the GPSC are schematically illustrated in Figure 15. When the northwestward-propagating F_{bc} emanating from the Hengchun Ridge impinges onto the Taiwan Banks, the reflected and incident waves may create a standing wave off the southwestern coast of Taiwan (Figure 15a). The second mechanism is that the southeastward F_{bc} generated by the barotropic tidal currents over the Taiwan Banks meets the northwestward F_{bc} from the Hengchun Ridge and forms partial internal standing tides off the GPSC (Figure 15b). The second mechanism seemingly contributes more significantly to the formation of the internal standing tides than does the first mechanism.

[25] Similar to the aforementioned formation processes, internal standing tides may occur inside the GPSC. Because the canyon length is approximately one-fourth of the incident internal wave, a quarter-wave resonance is also observed based on the co-oscillating tidal theory. The higher isopycnal vertical displacements near the canyon head (Figures 6 and 7), together with the smaller F_{bc} at the same region compared to those at the canyon mouth (Figure 9), are indicative of a standing internal wave. The canyon length of approximately 20 km is close to one-fourth of a semidiurnal baroclinic tide wavelength in the canyon, favoring a near resonance condition in the GPSC. However, it is rare to form a purely standing wave in the GPSC because the incident baroclinic energy does not seem to be fully reflected at the canyon head and because of the S-like, rather than straight, thalweg of the canyon. Nevertheless, the baroclinic energy is enhanced in the GPSC, presumably due to the partial standing baroclinic

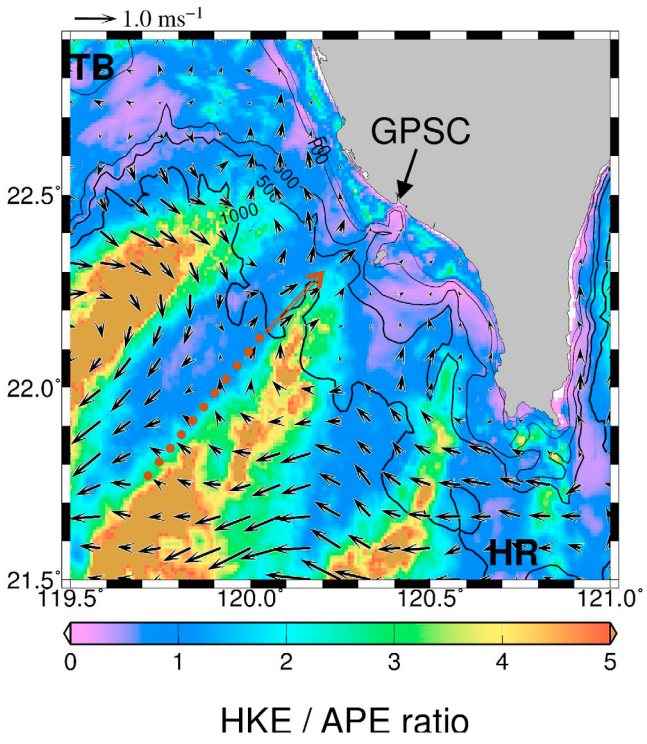

Figure 14. The time mean (seven days), depth-integrated *HKE* and APE ratio and associated C_g (black vectors). The dashed line indicates the band of $HKE \approx APE$.

tides outside the canyon and the nearly quarter-wave resonance of baroclinic tides in the canyon.

4.4. Enhancement of Vertical Mixing

[26] Baroclinic tides can be focused as they approach the head and bottom of a submarine canyon [*Gordon and Marshall*, 1976; *Hotchkiss and Wunsch*, 1982]. Consequently, the vertical mixing could be enhanced in canyons, such as Monterey Canyon, where the diapycnal diffusivity within 10 km of the canyon head is among the highest observed anywhere (2.5×10^{-3} m^2 s^{-1}) [*Carter and Gregg*, 2002; *Gregg et al.* 2005]. *Gregg et al.* [2011] further used the observational data to analyze and POM to simulate the barotropic and baroclinic tides in Ascension Canyon of Monterey Bay and found that the averaged diapycnal diffusivity is 3.9×10^{-3} m^2 s^{-1}, which is greater than that in Monterey Canyon. Based on the model results, the authors concluded that no major sources were feeding baroclinic energy into the canyon, but the authors determined that significant energy is exchanged between barotropic and baroclinic flows along the tops of the sides, where the slopes are critical.

[27] In the GPSC, 10.1 MW of baroclinic tidal energy is dissipated, as estimated from model results. The turbulence kinetic energy dissipation rate per unit water mass, ε, averaged within the GPSC (the rectangle in Figure 13), is approximately 2.76×10^{-7} W kg^{-1}, which is similar to that in the Luzon Strait [*Jan et al.*, 2008] and is a factor 100 greater than that in the open ocean. The vertical eddy diffusivity can be computed using Osborn's formulation, which is defined as $K_\rho = 0.2\varepsilon N^{-2}$ [*Osborn*, 1980]. Given the depth averaged buoyancy frequency, $N = 0.004$ s^{-1}, a bulk estimate of K_ρ is 3.5×10^{-3} m^2 s^{-1}, which is O(100) times that in the abyssal ocean with a typical internal wavefield [*Toole et al.*, 1994; *Lien and Gregg*, 2001]. The estimated vertical diffusivity is similar to that calculated from the hydrographic data for the Luzon Strait [*Qu et al.*, 2006] and that in Ascension Canyon of Monterey Bay [*Gregg et al.*, 2011].

[28] The relatively high rate of turbulence mixing potentially facilitates the re-suspension of sediments in the GPSC. Figure 2c shows the light transmission in %, which was measured simultaneously with the CTD cast at station G1 during 4–5 September, 2010. A pronounced benthic nepheloid layer, which is similar to that described by *Liu et al.* [2009], is seen in Figure 2c. The strong turbulent mixing induced by the baroclinic tides is responsible for the near-bottom nepheloid layer formation. Importantly, another distinct surface nepheloid layer is seen near the bottom of the surface mixed layer, suggesting that the pycnocline may be a barrier inhibiting the entrainment and the downward deposition of the suspended sediments. Further discussion on the dynamics of the nepheloid layers is beyond the scope of this study.

5. Summary and Concluding Remarks

[29] The GPSC serves as a conduit for the exchange of river-borne and oceanic materials off the southwestern coast of Taiwan. The energetic baroclinic tides in the canyon dominate the physical process of material exchange, which may also exert a sizable influence on the geological and biological processes in the GPSC because of the enhancement of upwelling and vertical mixing in addition to the associated re-suspension process. This study examined the physical processes of baroclinic tides by using a three-dimensional model driven by four principal tidal constituents, namely, O_1, K_1, M_2 and S_2, which were blended together in an area covering the Luzon Strait and the southeastern Taiwan Strait. The model-produced baroclinic tides agreed reasonably well with the observations in the GPSC in mag-

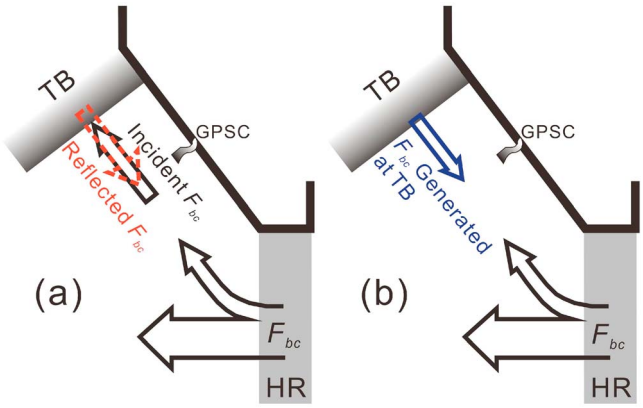

Figure 15. (a and b) Schematic diagrams showing the potential mechanisms for the formation of internal standing waves off the GPSC. Black arrows represent F_{bc} generated on Hengchung Ridge (HR). The red arrow in Figure 15a represents the reflected F_{bc} of the incident F_{bc} from HR; the blue arrow in Figure 15b indicates F_{bc} directly generated at the Taiwan Banks (TB).

nitudes of tidal current velocity, isotherm vertical displacement and baroclinic tidal energy flux. According to results derived from the simulations, the time mean, depth-integrated, baroclinic tidal energy flux is 2.2 kW m^{-1} along the canyon, which is comparable to that computed from the CTD and shipboard ADCP data of this study and to that observed in Monterey Canyon. The time-mean area-integrated baroclinic energy in the GPSC is 189.4 MW. The energetic baroclinic tides lead to a relatively high vertical diffusivity of 3.5×10^{-3} m^2 s^{-1} in the section close to the head of the GPSC.

[30] Results from numerical experiments indicate that the spring-neap cycle of the baroclinic tidal energy in the GPSC lags behind that over the Hengchun Ridge by approximately 25-h. This finding suggests that the baroclinic tidal generation on the two meridional ridges in the Luzon Strait, in addition to that on the steep topography in the southeastern Taiwan Banks, are major sources of baroclinic tidal energy flux propagating into the GPSC. Only 4.4% of the total baroclinic energy is generated on the steep topography in the GPSC, thereby suggesting that the local generation of the baroclinic energy is minor. The other 95.6% of the total baroclinic energy is remotely generated, of which 40.7% is propagating mode and 54.9% is standing mode. For the propagating mode, 31.9% of the total baroclinic energy in the GPSC is from the Luzon Strait and 8.8% of the total value from the southern flank of the Taiwan Banks. The northwestward and southeastward baroclinic energy beams radiating from the Luzon Strait and the southern Taiwan Strait, respectively, meet each other and form internal partial standing tides off the GPSC. The transverse baroclinic energy, where $HKE \approx APE$ of the internal partial standing tides, propagates toward the GPSC and provides the remaining 54.9% of the total baroclinic tidal energy in the GPSC.

[31] The physical processes in the GPSC have rarely been studied with numerical models in the open literature. To resolve the dynamics of the baroclinic tides in the GPSC more clearly, the model domain must be large enough to include the Luzon Strait, but must sacrifice the horizontal grid resolution for the canyon. The lack of baroclinic tidal energy from the Luzon Strait significantly underestimates the baroclinic energy flux in the GPSC. This study, although bearing certain limitations of the present model, serves as a moderate start toward future interdisciplinary modeling studies.

[32] **Acknowledgments.** This study was financially sponsored by the National Science Council (NSC) of Taiwan, Republic of China under grant NSC98-2611-M-002-019-MY3. The NSC's Ocean Data Bank provided 500 m resolution bathymetry data and the CTD data. The captain, crew, and resident technicians of R/V *Ocean Researcher*-I helped the measurement described in this study. T.-S. Kuo helped process the Sb-ADCP, LADCP, and the CTD data. Two anonymous reviewers contributed substantially to the improvement of the paper.

References

Alford, M. H., M. C. Gregg, and M. A. Merrifield (2006), Structure, propagation, and mixing of energetic baroclinic tides in Mamala Bay, Oahu, Hawaii, *J. Phys. Oceanogr.*, *36*, 997–1018, doi:10.1175/JPO2877.1.

Allen, S. E., and X. D. de Madron (2009), A review of the role of submarine canyons in deep-ocean exchange with the shelf, *Ocean Sci.*, *5*, 607–620, doi:10.5194/os-5-607-2009.

Baines, P. G. (1982), On internal tide generation models, *Deep-Sea Res.*, *29*, 307–338, doi:10.1016/0198-0149(82)90098-X.

Blumberg, A. F., and L. H. Kantha (1985), Open boundary condition for circulation models, *J. Hydraul. Eng.*, *111*(2), 237–255, doi:10.1061/(ASCE)0733-9429(1985)111:2(237).

Blumberg, A. F., and G. F. Mellor (1987), A description of a three dimensional coastal ocean circulation model, in *Three-Dimensional Coastal Ocean Models*, *Coastal Estuarine Stud. Ser.*, vol. 4, edited by N. Heaps, pp. 1–16, AGU, Washington, D. C.

Carter, G. S. (2010), Barotropic and baroclinic M_2 tides in the Monterey Bay region, *J. Phys. Oceanogr.*, *40*, 1766–1783, doi:10.1175/2010JPO4274.1.

Carter, G. S., and M. C. Gregg (2002), Intense, variable mixing near the head of Monterey Submarine Canyon, *J. Phys. Oceanogr.*, *32*, 3145–3165, doi:10.1175/1520-0485(2002)032<3145:IVMNTH>2.0.CO;2.

Carter, G. S., M. A. Merrifield, J. M. Becker, K. Katsumata, M. C. Gregg, D. S. Luther, M. D. Levine, T. J. Boyd, and Y. L. Firing (2008), Energetics of M_2 barotropic-to-baroclinic tidal conversion at the Hawaiian islands, *J. Phys. Oceanogr.*, *38*, 2205–2223, doi:10.1175/2008JPO3860.1.

Chiou, W. D., C. C. Wu, and L. Z. Cheng (2000), Spatio-temporal distribution of sergestid shrimp *Acetes intermedius* in the coastal waters of southwestern Taiwan, *Fish. Sci.*, *66*, 1014–1025, doi:10.1046/j.1444-2906.2000.00163.x.

Chiou, W. D., L. Z. Cheng, and C. T. Chen (2003), Effects of lunar phase and habitat depth on vertical migration patterns of the sergestid shrimp *Acetes intermedius*, *Fish. Sci.*, *69*, 277–287, doi:10.1046/j.1444-2906.2003.00618.x.

Duda, T. F., J. F. Lynch, J. D. Irish, R. C. Beardsley, S. R. Ramp, C.-S. Chiu, T.-Y. Tang, and Y.-J. Yang (2004), Internal tide and nonlinear internal wave behavior at the continental slope in the northern South China Sea, *IEEE J. Oceanic Eng.*, *29*(4), 1105–1130, doi:10.1109/JOE.2004.836998.

Gordon, R. L., and N. F. Marshall (1976), Submarine canyons: Internal wave traps?, *Geophys. Res. Lett.*, *3*, 622–624, doi:10.1029/GL003i010p00622.

Gregg, M. C., G. S. Carter, and E. Kunze (2005), Corrigendum, *J. Phys. Oceanogr.*, *35*, 1712–1715, doi:10.1175/JPO2789.1.

Gregg, M. C., R. A. Hall, G. S. Carter, M. H. Alford, R.-C. Lien, D. P. Winkel, and D. J. Wain (2011), Flow and mixing in Ascension, a steep, narrow canyon, *J. Geophys. Res.*, *116*, C07016, doi:10.1029/2010JC006610.

Hall, R. A., and G. S. Carter (2011), Internal tides in Monterey Submarine Canyon, *J. Phys. Oceanogr.*, *41*, 186–204, doi:10.1175/2010JPO4471.1.

Haney, R. L. (1991), On the pressure gradient force over steep topography in sigma coordinate ocean models, *J. Phys. Oceanogr.*, *21*, 610–619, doi:10.1175/1520-0485(1991)021<0610:OTPGFO>2.0.CO;2.

Holloway, P. E., and M. A. Merrifield (2003), On the spring-neap variability and age of the internal tide at the Hawaiian Ridge, *J. Geophys. Res.*, *108*(C4), 3126, doi:10.1029/2002JC001486.

Hotchkiss, F. S., and C. Wunsch (1982), Internal waves in Hudson Canyon with possible geological implications, *Deep-Sea Res.*, *29*, 415–442, doi:10.1016/0198-0149(82)90068-1.

Hu, C.-K., C.-T. Chiu, S.-H. Chen, J.-Y. Kuo, S. Jan, and Y.-H. Tseng (2010), Numerical simulation of barotropic tides around Taiwan, *Terr. Atmos. Oceanic Sci.*, *21*(1), 71–84, doi:10.3319/TAO.2009.05.25.02(IWNOP).

Isobe, A., T. Kuramitsu, H. Nozaki, and P.-H. Chang (2007), Reliability of ADCP data detided with a numerical model on the East China Sea shelf, *J. Oceanogr.*, *63*, 135–141, doi:10.1007/s10872-007-0011-z.

Jachec, S. M., O. B. Fringer, M. G. Gerritsen, and R. L. Street (2006), Numerical simulation of internal tides and the resulting energetics within Monterey Bay and the surrounding area, *Geophys. Res. Lett.*, *33*, L12605, doi:10.1029/2006GL026314.

Jan, S., and C. T. A. Chen (2009), Potential biogeochemical effects from vigorous internal tides generated in the Luzon Strait: A case study at the southernmost coast of Taiwan, *J. Geophys. Res.*, *114*, C04021, doi:10.1029/2008JC004887.

Jan, S., C.-S. Chern, J. Wang, and S.-Y. Chao (2007), Generation of diurnal K_1 internal tide in the Luzon Strait and its influence on surface tide in the South China Sea, *J. Geophys. Res.*, *112*, C06019, doi:10.1029/2006JC004003.

Jan, S., R.-C. Lien, and C.-H. Ting (2008), Numerical study of baroclinic tides in Luzon Strait, *J. Oceanogr.*, *64*(5), 789–802, doi:10.1007/s10872-008-0066-5.

Jordi, A., A. Orfila, G. Basterretxea, and J. Tintoré (2005), Shelf-slope exchanges by frontal variability in a steep submarine canyon, *Prog. Oceanogr.*, *66*, 120–141, doi:10.1016/j.pocean.2004.07.009.

Kunze, E., L. K. Rosenfeld, G. S. Carter, and M. C. Gregg (2002), Internal waves in Monterey submarine canyon, *J. Phys. Oceanogr.*, *32*, 1890–1913, doi:10.1175/1520-0485(2002)032<1890:IWIMSC>2.0.CO;2.

Lee, I.-H., Y. H. Wang, J. T. Liu, W. S. Chuang, and J. Xu (2009a), Internal tidal currents in the Gaoping (Kaoping) submarine canyon, *J. Mar. Syst.*, *76*(4), 397–404, doi:10.1016/j.jmarsys.2007.12.011.

Lee, I.-H., R.-C. Lien, J. T. Liu, and W.-S. Chuang (2009b), Turbulent mixing and internal tides in Gaoping (Kaoping) Submarine Canyon, Taiwan, *J. Mar. Syst.*, *76*(4), 383–396, doi:10.1016/j.jmarsys.2007.08.005.

Lefèvre, F., C. Le Provost, and F. H. Lyard (2000), How can we improve a global ocean tide model at a regional scale? A test on the Yellow Sea and the East China Sea, *J. Geophys. Res.*, *105*(C4), 8707–8725, doi:10.1029/1999JC900281.

Lien, R. C., and M. C. Gregg (2001), Observations of turbulence in a tidal beam and across a coastal ridge, *J. Geophys. Res.*, *106*, 4575–4591, doi:10.1029/2000JC000351.

Liu, J. T., K. Liu, and J. C. Huang (2002), The effect of a submarine canyon on the river sediment dispersal and inner shelf sediment movements in southern Taiwan, *Mar. Geol.*, *181*, 357–386, doi:10.1016/S0025-3227(01)00219-5.

Liu, J. T., J. J. Hung, H. L. Lin, C. A. Huh, C. L. Lee, R. T. Hsu, Y. W. Huang, and J. C. Chu (2009), From suspended particles to strata: The fate of terrestrial substances in the Gaoping (Kaoping) submarine canyon, *J. Mar. Syst.*, *76*, 417–432, doi:10.1016/j.jmarsys.2008.01.010.

Lynch, L. F., S. R. Ramp, C.-S. Chiu, T.-Y. Tang, Y.-J. Yang, and J. A. Simmen (2004), Research highlights from the Asian Seas International Acoustics Experiment in the South China Sea, *IEEE J. Oceanic Eng.*, *29*(4), 1067–1074, doi:10.1109/JOE.2005.843162.

Martini, K. I., M. H. Alford, J. D. Nash, E. Kunze, and M. A. Merrifield (2007), Diagnosing a partly standing internal wave in Mamala Bay, Oahu, *Geophys. Res. Lett.*, *34*, L17604, doi:10.1029/2007GL029749.

Martinsen, E. H., and H. Engedahl (1987), Implementation and testing of a lateral boundary scheme as an open boundary condition in a barotropic ocean model, *Coastal Eng.*, *11*, 603–627, doi:10.1016/0378-3839(87)90028-7.

Matsumoto, K., T. Takanezawa, and M. Ooe (2000), Ocean tide models developed by assimilating TOPEX/POSEIDON altimeter data into hydrodynamical model: A global model and a regional model around Japan, *J. Oceanogr.*, *56*, 567–581, doi:10.1023/A:1011157212596.

Mellor, G. L., and T. Yamada (1982), Development of a turbulence closure model for geophysical fluid problems, *Rev. Geophys.*, *20*, 851–875, doi:10.1029/RG020i004p00851.

Mellor, G. L., T. Ezer, and L.-Y. Oey (1994), The pressure gradient conundrum of sigma coordinate ocean models, *J. Atmos. Oceanic Technol.*, *11*, 1126–1134, doi:10.1175/1520-0426(1994)011<1126:TPGCOS>2.0.CO;2.

Nash, J. D., E. Kunze, C. M. Lee, and T. B. Sanford (2006), Structure of the baroclinic tide generated at Kaena Ridge, Hawaii, *J. Phys. Oceanogr.*, *36*, 1123–1135, doi:10.1175/JPO2883.1.

Niwa, Y., and T. Hibiya (2004), Three-dimensional numerical simulation of M_2 internal tides in the East China Sea, *J. Geophys. Res.*, *109*, C04027, doi:10.1029/2003JC001923.

Osborn, T. R. (1980), Estimates of the local rate of vertical diffusion from dissipation measurements, *J. Phys. Oceanogr.*, *10*, 83–89, doi:10.1175/1520-0485(1980)010<0083:EOTLRO>2.0.CO;2.

Petruncio, E. T., J. D. Paduan, and L. K. Rosenfeld (2002), Numerical simulations of the internal tide in a submarine canyon, *Ocean Modell.*, *4*, 221–248, doi:10.1016/S1463-5003(02)00002-1.

Qu, T., J. B. Griton, and J. A. Whitehead (2006), Deepwater overflow throufh Luzon Strait, *J. Geophys. Res.*, *111*, C01002, doi:10.1029/2005JC003139.

Ramp, S. R., T.-Y. Tang, T. F. Duda, J. F. Lynch, A. K. Liu, C.-S. Chiu, F. L. Bahr, H.-R. Kim, and Y.-J. Yang (2004), Internal solitons in the northeastern South China Sea. Part I: Sources and deep water propagation, *IEEE J. Oceanic Eng.*, *29*(4), 1157–1181, doi:10.1109/JOE.2004.840839.

Rudnick, D. L., et al. (2003), From tides to mixing along the Hawaiian Ridge, *Science*, *301*, 355–357, doi:10.1126/science.1085837.

Smagorinsky, J. (1963), General circulation experiments with the primitive equations: Part I. The basic experiments, *Mon. Weather Rev.*, *91*, 99–164, doi:10.1175/1520-0493(1963)091<0099:GCEWTP>2.3.CO;2.

Toole, J. M., R. W. Schmitt, and K. L. Polzin (1994), Estimates of idapycnal mixing in the abyssal ocean, *Science*, *264*, 1120–1123, doi:10.1126/science.264.5162.1120.

Wang, J., and C. S. Chern (1996), Preliminary observation of internal surges in Tunk-Kang, *Acta Oceanogr. Taiwan*., *35*, 17–40.

Wang, Y. H., I.-H. Lee, and J. T. Liu (2008), Observation of internal tidal currents in the Kaoping Canyon off southwestern Taiwan, *Estuarine Coastal Shelf Sci.*, *80*(1), 153–160, doi:10.1016/j.ecss.2008.07.016.

H. Chien, Institute of Hydrological and Oceanic Sciences, National Central University, 300 Jungda Rd., Jungli 32001, Taiwan.

M.-D. Chiou, S. Jan, and J. Wang, Institute of Oceanography, National Taiwan University, No. 1, Sec. 4, Roosevelt Road, Taipei 10617, Taiwan. (senjan@ntu.edu.tw)

R.-C. Lien, Applied Physics Laboratory, University of Washington, 1013 NE 40th St., Box 355640, Seattle, WA 98105–6698, USA.